Acta Cryst. (1999). B**55**, 348–354

The crystal structure of the *B*-site ordered complex perovskite $Sr(Yb_{0.5}Nb_{0.5})O_3$

Jae Ho Yang,[a] Woong Kil Choo,[a]* Jin Ho Lee[b] and Chang Hee Lee[b]

[a]*Department of Materials Science and Engineering, Korea Advanced Institute of Science and Engineering, Taejon, Korea, and* [b]*Department of Neutron Physics, Hanaro Center, Korea Atomic Energy Research Institute, Taejon, Korea. E-mail: wkchoo@kaist.ac.kr*

(*Received 24 August 1998; accepted 22 December 1998*)

Abstract

The room-temperature crystal structure of the *B*-site ordered complex perovskite strontium ytterbium niobate, $Sr(Yb_{0.5}Nb_{0.5})O_3$ [monoclinic, $Z = 2$, $P2_1/n$ (set 2), $a = 5.79095\,(8)$, $b = 5.82210\,(7)$, $c = 8.20358\,(12)$ Å, $\beta = 90.126\,(1)^\circ$, with final $R_{wp} = 0.0595$, $R_{Bragg} = 0.0203$ for the neutron profile and $R_{wp} = 0.0832$, $R_{Bragg} = 0.0193$ for the X-ray profile, respectively], was determined by X-ray powder diffraction, high-resolution neutron powder diffraction and transmission electron microscopy. This compound shows a slight triclinic distortion from the prototype doubled cubic perovskite cell as a result of an $a^-a^-c^+$-type oxygen octahedral tilting distortion. It is also shown that the site ordering of the different species of *B*-site cations, Yb^{3+} and Nb^{5+}, inherently leads to a difference between the volumes of the YbO_6 and NbO_6 octahedra. This volume difference is shown to inevitably inhibit the rigid rotation of octahedra.

1. Introduction

Perovskite oxides are of widespread interest because of their wide-ranging physical and chemical properties. Furthermore, their crystal structures are directly relevant to physical properties such as ferroelectricity, antiferroelectricity, piezoelectricity, and optical activity, since these are directly influenced by ionic displacements.

The ideal structure of perovskite-type oxides (ABO_3, space group $Pm\bar{3}m$) is well known and very simple. In essence, the perovskite structure consists of a three-dimensionally linked network of BO_6 octahedra, with *A* cations filling the spaces between the octahedra. Various perovskite compounds in which the *B* sites are occupied by two cation species have been synthesized so far and their crystal structures have been determined (Galasso, 1990; Reaney *et al.*, 1994). They have the general chemical formula $AB'_xB''_{1-x}O_3$. Depending on their ionic radii and charges ordering of the cations may occur, giving rise to different crystal structures (Setter & Cross, 1980). The prototype structure of a perfectly ordered perovskite has a cubic unit cell with a doubled cell parameter around 8 Å and belongs to the face-centered space group $Fm\bar{3}m$ as a result of the NaCl-type B' and B'' cation ordering. Interestingly, this type of ordering is same as the Heusler alloy ordering that occurs in Cu_2MnAl. This metallurgical ordering type is often designated as $L2_1$ ordering (Jackson, 1991).

Although the ideal perovskite structure is cubic, the real structure often deviates from the cubic structure. Under topological and geometrical constraints, three structural degrees of freedom of distortion from the ideal cubic perovskite structure are considered to be possible: (i) displacements of the cations *A* and *B* from the centers of the polyhedra, (ii) distortion of the anion octahedra and (iii) tilting of the BO_6 octahedra. The displacement of the cations and the distortion of the octahedra are usually correlated and driven by electronic instability of the metal cations. The Jahn–Teller distortion in $KCuF_3$ (Okazaki & Snemune, 1961) and the cation displacement in $PbZrO_3$ (Corker *et al.*, 1997) are typical examples. Octahedral tilting, a more common distortion mechanism, can be realized by tilting the rigid BO_6 octahedra while maintaining their corner-sharing connectivity. This type of distortion is typically observed when the *A* cation is too small for the cubic BO_6 corner-sharing octahedral network. Moreover, there is some hierarchy of tilting with the volume difference of the *A* cation and the BO_6 octahedra. The structural changes accompanied by octahedral tilting attract great attention because they have important effects on several physical properties; the temperature dependence of the dielectric constant in low-dielectric-loss materials (Bosman & Havinga, 1963; Colla *et al.*, 1993), the change of magnetoresistance in $LaMnO_3$ with *A*-cation substitution (Hwang *et al.*, 1995; Fontcuberta *et al.*, 1996) and the symmetry change between the rhombohedral and orthorhombic structure with *A*-cation substitution in the ceramic fuel-cell material $LaCrO_3$ (Minh, 1993) are typical examples.

Octahedral tilting in perovskites was first examined by Megaw & Darlington (1975); the fundamental work was carried out by Glazer (1972, 1975). The latter demonstrates that the space group can be largely determined by the pattern of in-phase (a^+), anti-phase (a^-), and null (a^0) octahedral tilting along one of the Cartesian coordinate axes. Furthermore, a classification of octahedral tilting in terms of 23 alternative tilt

systems was proposed. Regular BO_6 octahedra were assumed, with all the tilts considered as combinations of component tilts about the three pseudocubic axes. However, Leinenweber & Parise (1995) recently found that the space group which results from $a^+a^+c^-$ tilting was not coincident with Glazer's prediction. This disagreement is caused by the assumption of rigid BO_6 rotation. More recently, Woodward (1997*a*) has demonstrated that in several tilt systems it is not possible to link together a three-dimensional network of perfectly rigid octahedra. In these tilt systems a small distortion of the octahedra must occur. In addition, Woodward also predicted the space groups that arise from the combination of octahedral tilting and *B*-site cation ordering. When the two bond distances are nonequivalent, this can also inhibit the rigid rotation of octahedra in the interconnected $B'O_6$ and $B''O_6$ network in certain tilt systems.

Another approach, concerning the structure-stabilizing force associated with the octahedral tilting, has been proposed by several researchers. Thomas (1989, 1996) compared the relative stabilities of cubic ($a^0a^0a^0$), rhombohedral ($a^-a^-a^-$), and orthorhombic ($a^-a^-a^+$) perovskites, based on the polyhedral volume ratio of the *A*-cation cuboctahedra and the *B*-cation octahedra. It was concluded that the polyhedral volume of the *A* cation could be maximized, thereby reducing anion–anion repulsion in the orthorhombic structure, as the tilt angle increases. Woodward (1997*b*) investigated and compared the various tilt systems, and found that those tilt systems in which all of the *A*-cation sites remain crystallographically equivalent are strongly favored. In particular, based on both ionic- and covalent-model energy calculations, the orthorhombic $a^-a^-a^+$ system was found to give the lowest energy structure because it maximizes the number of short *A*—O bonds.

The strontium ytterbium niobate $Sr(Yb_{0.5}Nb_{0.5})O_3$ basically has a *B*-site ordered complex perovskite structure. It has potentially excellent high-frequency dielectric properties (Takata & Kageyama, 1989) and a yet more excellent capability for high-frequency applications upon forming solid solutions. It is known that the dielectric loss in perovskite oxides can be reduced by *B*-site ordering and the temperature dependence of the dielectric constant is greatly affected by the nature of the octahedral tilting. Thus it is important to understand the structure of *B*-site ordered complex perovskites. Although the crystal structures of simple prototype perovskites have been investigated rather thoroughly, the crystal structure of *B*-site ordered complex perovskites has not yet been studied as closely. In this paper we present a detailed determination of the structure of $Sr(Yb_{0.5}Nb_{0.5})O_3$ by neutron powder diffraction, X-ray powder diffraction and transmission electron microscopy. In particular, we will focus our attention on the effect of *B*-site Yb^{3+}/Nb^{5+} cation ordering on the octahedral tilting distortion.

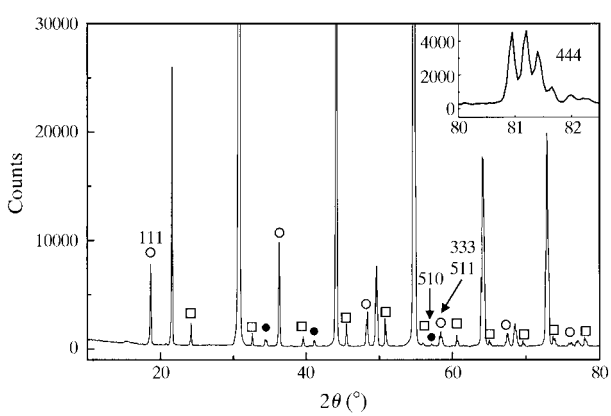

Fig. 1. The room-temperature X-ray diffraction profile of $Sr(Yb_{0.5}Nb_{0.5})O_3$. Open circles, filled circles, and open squares represent *R*-mode, *M*-mode, and *X*-mode reflections, respectively.

2. Experimental

It is difficult to obtain single-phase ceramic samples of $Sr(Yb_{0.5}Nb_{0.5})O_3$ by conventional solid-state reaction. Therefore, calcined powders of $Sr(Yb_{0.5}Nb_{0.5})O_3$ were prepared by a wet chemical method using $Sr(NO_3)_2$, $Yb_2(NO_3)_2$, Nb_2Cl_5 and citric acid as starting materials. Details of this process will be published elsewhere.

Transmission electron microscopy (TEM) selected-area diffraction patterns (SADPs) were obtained on ion-beam-thinned sections using a Philips CM20/T electron microscope. X-ray powder diffraction patterns were collected at room temperature up to $\sin(\theta_{max})/\lambda = 0.532$ Å^{-1} on a Rigaku Rotaflex diffractometer using Cu $K\alpha$ radiation and a graphite monochromator. The neutron powder diffraction pattern was collected at room temperature on a high-resolution powder diffractometer (HRPD) [$\lambda = 1.8339$ Å and $\sin(\theta_{max})/\lambda = 0.527$ Å^{-1}] at the HANARO reactor, Korea Atomic Energy Research Institute (KAERI). Neutrons from the ST2 channel of the reactor were monochromated by a vertically focusing composite Ge monochromator at the 90° take-off position.

Structure refinements were carried out by fitting the combined X-ray and neutron profiles using the Rietveld method and the program *RIETAN* (Kim & Izumi, 1994). The lattice parameters, fractional coordinates, and displacement parameters of the cations were determined by Rietveld refinement of the X-ray profile. The fractional coordinates and displacement parameters of the O atoms were determined from the neutron profile. The preliminary coordinates and displacement parameters for the cations were used in the neutron-profile refinement and those of O atoms were used in an X-ray-profile refinement and *vice versa* until the final refinements converged.

3. Results

3.1. *The characterization of reflection lines*

Figs. 1 and 2 show the X-ray and neutron diffraction profiles, respectively, of $Sr(Yb_{0.5}Nb_{0.5})O_3$ at room temperature. In addition to the fundamental reflection lines of a typical simple perovskite, several sets of extra diffraction lines indicating the formation of a larger superlattice structure are also observed. In particular, the fundamental peaks at high 2θ angle are split, implying a deviation from cubic symmetry. In addition,

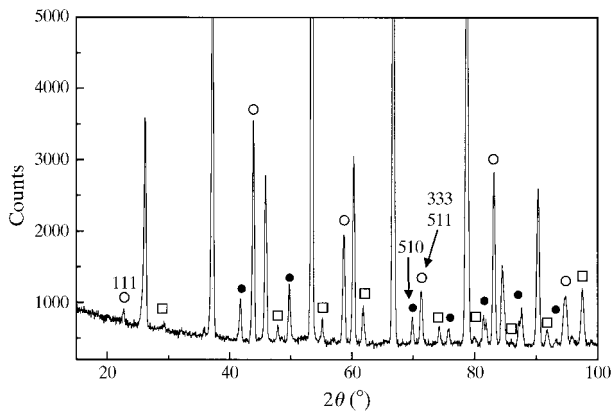

Fig. 2. The room-temperature neutron diffraction profile of $Sr(Yb_{0.5}Nb_{0.5})O_3$. See Fig. 1 for symbols.

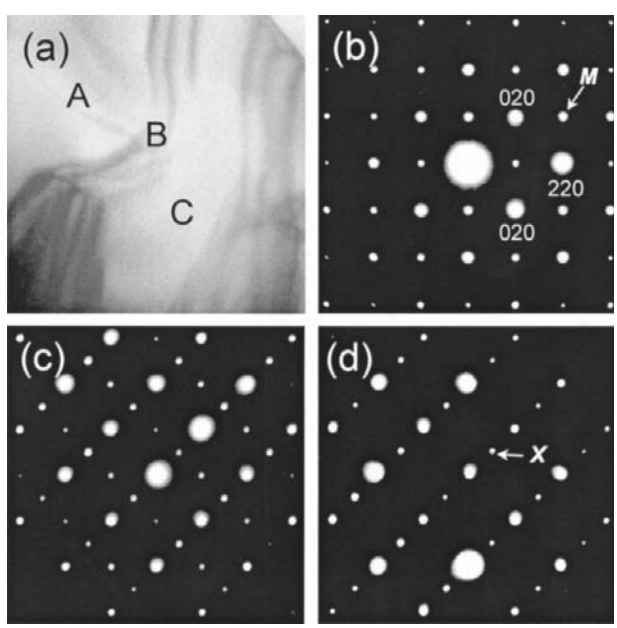

Fig. 3. (*a*) A TEM micrograph of $Sr(Yb_{0.5}Nb_{0.5})O_3$ and (*b*), (*c*), and (*d*) SADPs taken from the regions *A*, *B* and *C* as shown in (*a*); (*b*) shows the $[001]_p$ zone, (*c*) shows the $[001]_p/[010]_p$ (or $[100]_p$) zones and (*d*) shows the $[010]_p$ (or $[100]_p$) zone. The *X* mode can only be observed in (*d*) and the *M* mode can only be observed in (*b*). Note: the (110) diffraction spots in (*b*) are double diffractions of *M*-mode superlattice spots.

Table 1. *Refined fractional atomic coordinates and displacement parameters (Å^2) for monoclinic $Sr(Yb_{0.5}Nb_{0.5})O_3$ obtained by combined X-ray and neutron profile analysis*

The coordinates and displacement parameters of the cations were determined using the X-ray profile and those of the O atoms were determined using the neutron profile. The displacement factor expression is $\exp(-B\sin^2\theta/\lambda^2)$.

	x	*y*	*z*	*B*
Sr	0.005 (1)	0.0271 (3)	0.2511 (7)	0.66 (4)
Yb	1/2	0	0	0.32 (4)
Nb	0	1/2	0	0.26 (6)
O1	0.199 (2)	0.773 (2)	0.037 (2)	0.66 (6)
O2	0.270 (2)	0.301 (2)	0.035 (2)	0.66 (6)
O3	0.430 (2)	0.015 (1)	−0.262 (2)	0.66 (6)

R_{wp} (neutron) = 0.0595 R_{wp} (X-ray) = 0.0832
R_{Bragg} (neutron) = 0.0203 R_{Bragg} (X-ray) = 0.0193

the highest *d*-value reflection line appears near the body center of the reciprocal lattice of a simple perovskite. Either $L2_1$ ordering of *B*-site cations or anti-phase tilting of oxygen octahedra can produce these types of reflections. It is believed that these two factors contribute to the reflections of $Sr(Yb_{0.5}Nb_{0.5})O_3$ simultaneously. (This is discussed below.) The presence of *F*-centering reflections caused by *B*-site ordering suggests that the prototypic crystal has an effectively doubled unit cell ($2a_s \times 2a_s \times 2a_s$) along all the crystallographic axis directions of a simple perovskite cell ($a_s \times a_s \times a_s$), where the subscript *s* denotes the simple cubic perovskite.

Along these lines, the extra reflections may be classified into the three groups: (i) $\{h + 1/2, k + 1/2, l\}_p$, (ii) $\{h, k, l + 1/2\}_p$ and (iii) $\{h + 1/2, k + 1/2, l + 1/2\}_p$, which are denoted by filled circles, open squares, and open circles, respectively, in Fig. 1 and Fig. 2. The subscript *p* denotes the prototype doubled perovskite. These reflection indices correspond to multiples of the *M* point, the *X* point and the *R* point of the first Brillouin zone of a simple perovskite. So, for convenience, we will call the three groups of reflections the *M*-mode, the *X*-mode and the *R*-mode reflections, respectively.

The modulation-vector relationship between the *M* and *X* modes can be found in the $[001]_p$ and $[100]_p/[010]_p$ zones of TEM SADPs. Fig. 3(*a*) is a TEM micrograph. Figs. 3(*b*), (*c*), and (*d*) are the SADPs obtained for the three regions *A*, *B* and *C* shown in Fig. 3(*a*), respectively. From these figures, we can easily find the *M* mode (Fig. 3*b*) and *X* mode (Fig. 3*d*). However, these two superlattice patterns cannot appear in the same plane and they must be perpendicular to each other. So, if we index the *M*-mode reflections as $(h + 1/2, k + 1/2, l)_p$, the *X*-mode reflections must be alternately indexed as $(h, k, l + 1/2)_p$. Fig. 3(*c*) shows the superimposed patterns of Fig. 3(*b*) and 3(*d*), therefore the *B* region is subdivided by 90° domain boundaries.

In general, the *M*-mode and *R*-mode reflections have much higher relative intensities in the neutron profile than in the X-ray profile, except for the $(111)_p$ reflection. This means that these two modes are tied to oxygen-related superlattice reflections, *i.e.* in-phase and anti-phase tilting of the oxygen octahedra, respectively.

Interestingly enough, the neutron intensity of the $(333)_p$ ordering reflection is much larger than that of the $(111)_p$ ordering reflection and *vice versa* in X-ray diffraction. Inferring from the $(111)_p$ and $(333)_p$ X-ray reflections, Fig. 1, the intensity of the latter ought to be much smaller. It happens that the interplanar spacing corresponding to the *R*-mode $(511)_p$ reflection is virtually same as that of $(333)_p$. Hence these two reflections overlap. This is why the $(333)_p$ neutron reflection combined with the $(511)_p$ reflection in Fig. 2 is much larger than that of $(111)_p$. Furthermore, the much larger $(333)_p/(511)_p$ reflection intensity than the in-phase-tilting $(510)_p$ reflection intensity implies that there are indeed two anti-phase tilting axes. From the above results, we can infer that $Sr(Yb_{0.5}Nb_{0.5})O_3$ may be considered to be an $a^-a^-a^+$-type oxygen octahedron tilting system.

In the case of $CaTiO_3$, which shows an $a^-a^-a^+$ tilting, the Ca ion is forced to move along the $<110>_p$ direction in antiparallel sheets perpendicular to the $[001]_p$ axis (Glazer, 1975). The existence of an *X* mode in $Sr(Yb_{0.5}Nb_{0.5})O_3$ can be explained by the same structural consideration as in $CaTiO_3$. This fact coincides with the results of TEM investigation and acts as further evidence of the $a^-a^-a^+$ tilting.

3.2. *Determination of the space group and refinements*

As shown by the splitting of the 444 perovskite fundamental line into three, as shown clearly in the inset to Fig. 1, the lowering of the symmetry occurs by a triclinic distortion of the prototypic cubic cell. This triclinic cell can be converted to a primitive monoclinic cell with lattice parameters a_m = 5.791, b_m = 5.822, c_m = 8.204 Å, β = 90.12°; this cell indexes all the observed peaks satisfactorily. The monoclinic basis vectors of the room-temperature unit cell have the following relationship to the basis vectors of the prototype phase: $\mathbf{a}_m = \frac{1}{2}(\mathbf{a}_p + \mathbf{b}_p)$, $\mathbf{b}_m = \frac{1}{2}(-\mathbf{a}_p + \mathbf{b}_p)$, and $\mathbf{c}_m = \mathbf{c}_p$. The space-group determination is rather complicated and difficult. However, we can find an expected extinction rule based on consideration of the prototypic cell indexing and the lattice relationship between the prototype cell and the monoclinic unit cell. For example, the reflection indexes according to the prototype cell have only even-even-even-, odd-odd-

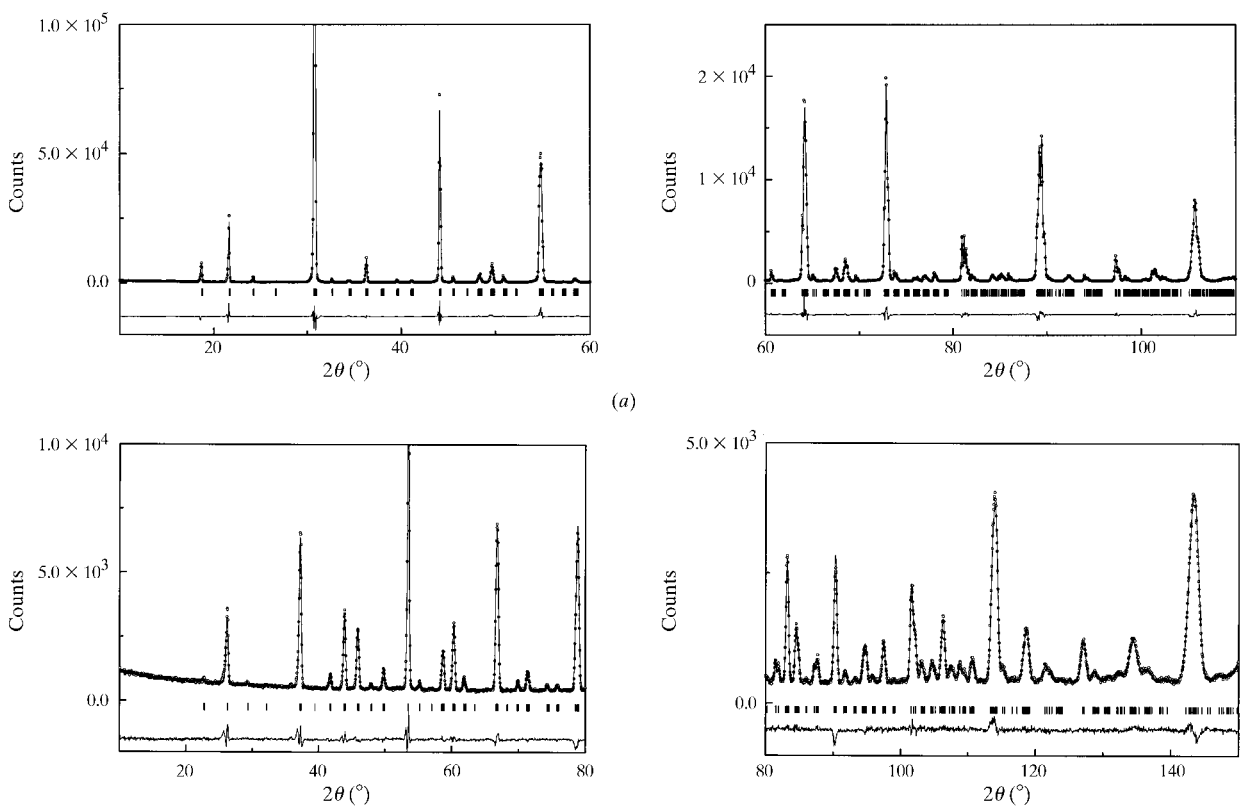

Fig. 4. (*a*) X-ray and (*b*) neutron diffraction powder patterns (circles: observed; line: calculated) with the difference profiles shown below.

Table 2. *Bond lengths (Å) and angles (°) between B-site cations and O atoms in the two different BO_6 octahedra*

Standard uncertainties are given in parentheses. The quadratic elongation λ is given by $\lambda = \sum_{i=1}^{n}(l_i/l_o)^2/n$ and the bond-angle variance σ is given by $\sigma = \sum_{i=1}^{n}(\theta_i - \theta_o)^2/(n-1)$ where l_o and θ_o are the cation–anion bond lengths and cation–anion–cation bond angles in regular coordination polyhedra, respectively, and l_i and θ_i are the cation–anion bond lengths and cation–anion–cation bond angles of the ith bond (Robinson *et al.*, 1971).

NbO_6 octahedron		YbO_6 octahedron	
$Nb-O1^{i}$, $Nb-O1^{ii}$	1.984 (10)	$Yb-O1^{iii}$, $Yb-O1^{iv}$	2.209 (9)
$Nb-O2^{i}$, $Nb-O2^{ii}$	1.969 (9)	$Yb-O2^{i}$, $Yb-O2^{v}$	2.219 (9)
$Nb-O3^{vi}$, $Nb-O3^{vii}$	1.994 (13)	$Yb-O3^{i}$, $Yb-O3^{v}$	2.191 (12)
$O1^{i}-Nb-O1^{ii}$, $O2^{i}-Nb-O2^{ii}$, $O3^{vi}-Nb-O3^{vii}$	180	$O1^{iii}-Yb-O1^{iv}$, $O2^{i}-Yb-O2^{v}$, $O3^{i}-Yb-O3^{v}$	180
$O1^{i}-Nb-O2^{i}$, $O1^{ii}-Nb-O2^{ii}$	89.26 (58)	$O1^{iii}-Yb-O2^{i}$, $O1^{iv}-Yb-O2^{v}$	88.98 (53)
$O1^{i}-Nb-O2^{ii}$, $O1^{ii}-Nb-O2^{i}$	90.74 (58)	$O1^{iv}-Yb-O2^{i}$, $O1^{iii}-Yb-O2^{v}$	91.02 (53)
$O1^{i}-Nb-O3^{vii}$, $O1^{ii}-Nb-O3^{vi}$	89.54 (48)	$O1^{iii}-Yb-O3^{i}$, $O1^{iv}-Yb-O3^{v}$	90.77 (40)
$O1^{i}-Nb-O3^{vi}$, $O1^{ii}-Nb-O3^{vii}$	90.46 (48)	$O1^{iii}-Yb-O3^{v}$, $O1^{iv}-Yb-O3^{i}$	89.23 (40)
$O2^{i}-Nb-O3^{vii}$, $O2^{ii}-Nb-O3^{vi}$	90.39 (59)	$O2^{i}-Yb-O3^{i}$, $O2^{v}-Yb-O3^{v}$	89.19 (44)
$O2^{i}-Nb-O3^{vi}$, $O2^{ii}-Nb-O3^{vii}$	89.61 (59)	$O2^{i}-Yb-O3^{v}$, $O2^{v}-Yb-O3^{i}$	90.81 (44)
Volume ($Å^3$)	10.4006	Volume ($Å^3$)	14.3428
Quadratic elongation	1.0001	Quadratic elongation	1.0003
Bond-angle variance	0.2450	Bond-angle variance	0.9595

Symmetry codes: (i) x, y, z; (ii) $-x, 1-y, -z$; (iii) $x, y-1, z$; (iv) $1-x, 1-y, -z$; (v) $1-x, -y, -z$; (vi) $-\frac{1}{2}+x, \frac{1}{2}-y, \frac{1}{2}+z$; (vii) $\frac{1}{2}-x, \frac{1}{2}+y, -\frac{1}{2}-z$.

even- (with $h \neq k$), odd-odd-odd-, and even-even-odd-type indexes ($a^-a^-a^+$ tilt system). So, k must be $2n$ for $(0k0)_m$. Concerning the tilt system and crystal system as mentioned above, the space group $P2_1/n$ (No. 14, set 2) can explain fully the observed profiles and predict the extinctions. This result coincides with that of Woodward's work on the crystal structure of ordered perovskites, in which the space groups of all the tilt systems with 1:1 *B*-site ordering were simulated. According to Woodward, the space group of the $a^-a^-a^+$-type-tilt ordered perovskite is $P2_1/n$. Our refinements were performed in accord with this space group. The Yb^{3+} and Nb^{5+} cations locate themselves in the rigid center of the octahedra in this space group.

The refined lattice parameters of the monoclinic cell are a = 5.79095 (8), b = 5.82210 (7), c = 8.20358 (12) Å, β = 90.126 (1)° The final atomic coordinates and displacement factors are listed in Table 1. We find that

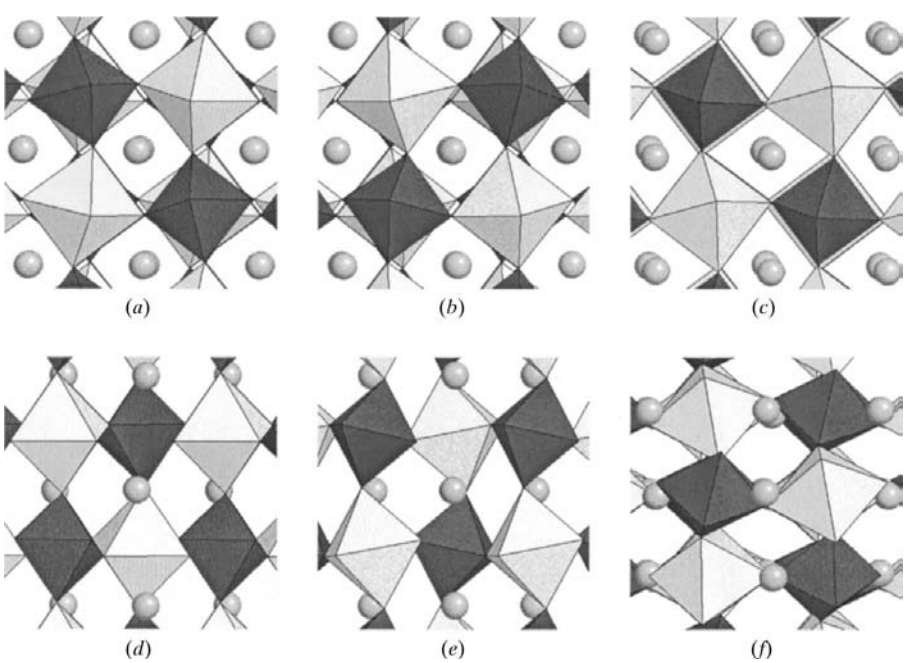

Fig. 5. Crystal-structure projections of $Sr(Yb_{0.5}Nb_{0.5})O_3$ on (*a*) $(1\bar{1}0)_m$, (*b*) $(110)_m$, (*c*) $(001)_m$, (*d*) $(100)_m$, (*e*) $(010)_m$, and (*f*) $(112)_m$. These viewing zones correspond to $(100)_p$, $(010)_p$, $(001)_p$, $(1\bar{1}0)_p$, $(110)_p$, and $(011)_p$ with respect to the prototypic crystal system, respectively.

the space group $P2_1/n$ defines the room-temperature crystal structure of $Sr(Yb_{0.5}Nb_{0.5})O_3$ well. The calculated profile fits to the experimental neutron and X-ray intensity data and the difference profiles for the refinements are shown in Fig. 4.†

4. Discussion and concluding remarks

In general, the *B*-site cation ordering is enhanced when the ionic size or the valence difference of the *B*-site ions is large. This means that the cation–anion bond lengths associated with each of the two *B*-site cations (Yb^{3+}/Nb^{5+}) are necessarily different. Consequently, the volumes of the two adjacent octahedra must also be different in $Sr(Yb_{0.5}Nb_{0.5})O_3$.

Fig. 5 shows a schematic view of the room-temperature structure of $Sr(Yb_{0.5}Nb_{0.5})O_3$, based on Table 1. The darker octahedra are NbO_6 and the lighter ones are YbO_6. The $a^-a^-a^+$ tilt system is clearly shown in Figs. 5(*a*)–(*c*). The anti-phase tilting angles are about 7° for YbO_6 and 8° for NbO_6. The in-phase tilting angles are about 1° larger than the anti-phase tilting angles. In addition to this, the volume difference between the NbO_6 and YbO_6 octahedra is also confirmed. Table 2 shows the *B*—O bond lengths and O—*B*—O bond angles in the YbO_6 and NbO_6 octahedra. We can clearly see that the *B*—O bond lengths vary and the O—*B*—O bond angles deviate from 90°. The octahedral distortions can also be caused by the difference in the volume of the NbO_6 and YbO_6 octahedra. The YbO_6 distortion can mainly accommodate the structural imperfection caused by the rigid rotation of the octahedra. This is because the deformations of the long Yb—O bond are more energetically and geometrically favored than those of the tightly bound short Nb—O bond. There are three types of O atom; they are shown in projection on the (001) plane in Fig. 6.

It is also worth noting the nature of the Yb—O3—Nb bond, where O3 lies on the in-phase tilting axis. In this bond, as we can infer from Table 2, the O atoms are more centrally located than in the others. It is seen that the Sr cation forces all O3 atoms to be located in the same plane, thereby minimizing the energy. This can be understood partly by considering the change in the geometry of the Sr—O bonds when tilting occurs. As shown in Fig. 7, the Sr—O bond lengths and the O3···O3 repulsion force can be reduced by locating the Sr and O3 ions in same plane. However, this increases the Nb—O bond length while decreasing that of Yb—O, thereby reducing the Madelung energy. Thus, the optimal position of O3 is determined by considering these two effects. These kinds of elongations and reductions also distort the octahedra. The tendency for coplanarity may affect the nature of the displacement of the *A*-site cation in ordered perovskites where spontaneous displacements exist, as in the Pb-based complex perovskites.

We have presented here the structure of monoclinic $Sr(Yb_{0.5}Nb_{0.5})O_3$, detemined by the analysis and refinement of X-ray and neutron profiles with the aid of TEM SADPs. It is revealed that the room-temperature structure has the $a^-a^-a^+$-type tilt system. Moreover, the difference in volume between the two oxygen octahedra caused by site ordering of Yb^{3+} and Nb^{5+} disturbs the rigid rotation of the octahedra. A discussion of the geometric and energy considerations associated with the distorted octahedra has also been given.

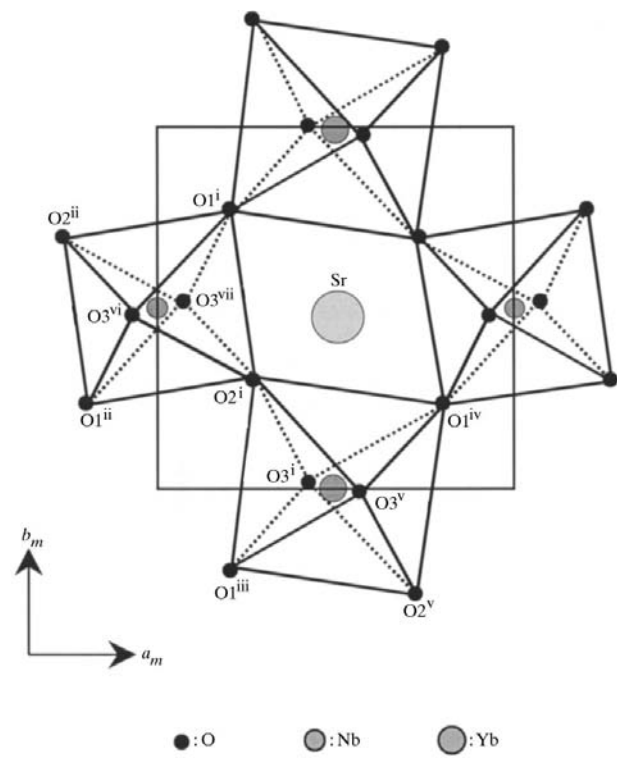

Fig. 6. A crystal-structure projection of $Sr(Yb_{0.5}Nb_{0.5})O_3$ on $(001)_m$. The three kinds of O atom are shown. Symmetry codes are given in Table 2.

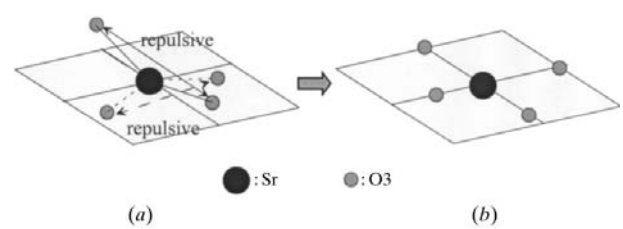

Fig. 7. Schematic representations of the Sr—O3 bond (*a*) when only tilting occurs, and (*b*) after deformation.

† Supplementary data for this paper are available from the IUCr electronic archives (Reference: SH0123). Services for accessing these data are described at the back of the journal.

References

Bosman, A. J. & Havinga, E. E. (1963). *Phys. Rev.* **129**, 1593–1600.

Colla, E. L., Reaney, I. M. & Setter, N. (1993). *J. Appl. Phys.* **74**, 3414–3425.

Corker, D. L., Glazer, A. M., Dec, J., Roleder, K. & Whatmore, R. W. (1997). *Acta Cryst.* B**53**, 135–142.

Fontcuberta, J., Martinez, B., Seffar, A., Pinol, S., Garcia-munoz, J. L. & Obradors, X. (1996). *Phys. Rev. Lett.* **76**, 1122–1125.

Galasso, F. S. (1990). *Perovskites and High T_c Superconductors.* New York: Gordon and Breach.

Glazer, A. M. (1972). *Acta Cryst.* B**28**, 3384–3392.

Glazer, A. M. (1975). *Acta Cryst.* A**31**, 756–762.

Hwang, H. Y., Cheong, S.-W., Radaelli, P. G., Marezio, M. & Batlogg, B. (1995). *Phys. Rev. Lett.* **75**, 914–917.

Jackson, A. G. (1991). *Handbook of Crystallography for Electron Microscopists and Others*, p. 117. New York: Springer-Verlag.

Kim, Y. I. & Izumi, F. (1994). *J. Ceram. Soc. Jpn*, **102**, 401–404.

Leinenweber, K. & Parise, J. (1995). *J. Solid State Chem.* **114**, 277–281.

Megaw, H. D. & Darlington, C. N. W. (1975). *Acta Cryst.* A**31**, 161–173.

Minh, N. Q. (1993). *J. Am. Ceram. Soc.* **76**, 563–588.

Okazaki, A. & Snemune, Y. (1961). *J. Phys. Soc. Jpn*, **28**, 443–446.

Reaney, I. M., Colla, E. I. & Setter, N. (1994). *Jpn. J. Appl. Phys.* **33**, 3984–3990.

Robinson, K., Gibbs, G. V. & Ribbe, P. H. (1971). *Science*, **172**, 567–570.

Setter, N. & Cross, L. E. (1980). *J. Appl. Phys.* **51**, 4356–4360.

Takata, M. & Kageyama, K. (1989). *J. Am. Ceram. Soc.* **72**, 1955–1959.

Thomas, N. W. (1989). *Acta Cryst.* B**45**, 337–344.

Thomas, N. W. (1996). *Acta Cryst.* B**52**, 16–31.

Woodward, P. M. (1997*a*). *Acta Cryst.* B**53**, 32–43.

Woodward, P. M. (1997*b*). *Acta Cryst.* B**53**, 44–66.